# Temporal variations in Holocene slip rate along the central Garlock fault, Pilot Knob Valley, California

**William M. Rittase[1,6], Eric Kirby[2,7], Eric McDonald[3], J. Douglas Walker[1], John Gosse[4], Joel Q.G. Spencer[5] and A.J. Herrs[1,8]**

[1]UNIVERSITY OF KANSAS, DEPARTMENT OF GEOLOGY, LAWRENCE, KANSAS 66045, USA
[2]PENNSYLVANIA STATE UNIVERSITY, DEPARTMENT OF GEOSCIENCES, UNIVERSITY PARK, PENNSYLVANIA 16802, USA
[3]DESERT RESEARCH INSTITUTE, RENO, NEVADA 89512, USA
[4]DALHOUSIE UNIVERSITY, DEPARTMENT OF EARTH SCIENCES, HALIFAX, NOVA SCOTIA, CANADA
[5]KANSAS STATE UNIVERSITY, DEPARTMENT OF GEOLOGY, MANHATTAN, KANSAS 66506, USA
[6]PRESENT ADDRESS: APACHE CORPORATION, HOUSTON, TEXAS 77056, USA
[7]PRESENT ADDRESS: OREGON STATE UNIVERSITY, COLLEGE OF EARTH, OCEAN AND ATMOSPHERIC SCIENCES, CORVALLIS, OREGON 97331, USA
[8]PRESENT ADDRESS: MARATHON OIL CORPORATION, HOUSTON, TEXAS 77056, USA

## ABSTRACT

Average geologic slip rates along the central Garlock fault, in eastern California, are thought to have been relatively steady at 5–7 mm/yr since at least the Late Pleistocene, yet present-day rates inferred from geodetic velocity fields are indistinguishable from zero. We evaluate the possibility of non-steady slip over millennial timescales using displaced Late Holocene alluvium along the central Garlock fault in Pilot Knob Valley. Truncation of a Late Holocene alluvial fan deposit against a shutter ridge requires a minimum of 30–37 m of displacement since deposition of the fan; maximum allowable displacement is 43–50 m. The extent of soil development atop the fan surface and optically stimulated luminescence ages bracket fan deposition between 3.5 and 4.5 ka. Together, these data require that slip rates during the Late Holocene were ~7–14 mm/yr, with a preferred rate of ~11–13 mm/yr. Our results, in conjunction with previous estimates of displacement over the past ~15 ka, require significant temporal variations in strain release along the Garlock fault and confirm previous suggestions that interactions among fault systems in eastern California give rise to alternating periods of fault activity and quiescence.

LITHOSPHERE; v. 6; no. 1; p. 48–58; GSA Data Repository Item 2014057 | Published online 17 January 2014 doi: 10.1130/L286.1

## INTRODUCTION

The temporal evolution of strain accumulation and release along intracontinental fault systems reflects a complicated interplay among far-field loading due to relative plate motions, changes in static (Coulomb) stress as a result of coseismic slip along nearby faults (e.g., Stein, 1999), changes in loading during post-seismic viscoelastic relaxation of the lower crust and/or upper mantle (e.g., Pollitz et al., 2001; Savage et al., 2003), and/or mechanical interactions between subjacent fault strands (e.g., Nicol et al., 2006). Recent high-resolution records of fault behavior provide mounting evidence that such interactions give rise to time-dependent slip histories along fault networks (e.g., Rockwell et al., 2000), yet the exact nature of these interactions remains obscure.

In eastern California, recent studies of slip rate and paleoearthquakes along N-NW-trending dextral faults reveal slip and paleoseismic histories that are strongly clustered in time (Rockwell et al., 2000; Oskin et al., 2008; Ganev et al., 2010); such behavior has been variously attributed to coordinated variations in activity between conjugate fault networks comprised by the Eastern California shear zone and the Garlock fault (Peltzer et al., 2001) or between the Eastern California shear zone and the San Andreas fault (Dolan et al., 2007). Although irregular paleoseismic records along the Garlock fault (e.g., McGill and Rockwell, 1998; Dawson et al., 2003) allow the possibility of time-variable displacement, such behavior is not yet apparent in measures of slip-rate integrated over multiple earthquake cycles. Current data indicates that the average slip rate over the past ~8–16 k.y. has been 5–7 mm/yr (McGill and Sieh, 1993; McGill et al., 2009; Ganev et al., 2012); data that could potentially constrain slip rates over shorter geologic time scales are limited (e.g., Helms et al., 2003).

Present-day velocity fields derived from geodetic measurements are at odds with relatively high rates of slip along the Garlock fault. Although the present day velocity field records right-lateral shear along the Eastern California shear zone, this zone appears to be continuous across the Garlock fault (Savage et al., 1990; Peltzer et al., 2001); the velocity field resolved parallel to the fault suggests sinistral displacement of only ~1–3 mm/yr (McClusky et al., 2001; Miller et al., 2001; Meade and Hager, 2005). In contrast, viscoelastic models of the fault network in eastern California that account for earthquake recurrence suggest that the present-day slip rate of the Garlock fault may be significantly higher, ranging from ~9–11 mm/yr (Chuang and Johnson, 2011), if the fault is late in the earthquake cycle (e.g., Savage and Prescott, 1978). Here we evaluate the hypothesis that slip along the Garlock fault has varied strongly in time during the Late Holocene. We utilize newly acquired, high-resolution topographic data from airborne laser swath mapping to reconstruct displacements along the central segment of the fault, and combine these with a chronology of alluvial deposits to determine slip rates.

## GEOLOGIC SETTING

Transcurrent deformation along the North America-Pacific plate boundary is accomplished by a combination of dextral slip along the San Andreas fault zone and distributed right-lateral shear along a network of faults in the Mojave Desert and east of the Sierra Nevada that together compose the Eastern California shear zone (Fig. 1). Embedded within this deforming crust is the Garlock fault, an ~250-km-long sinistral strike-slip fault that cuts across the northwest-trending Eastern California shear zone and terminates against the San Andreas system (Davis and Burchfiel, 1973).

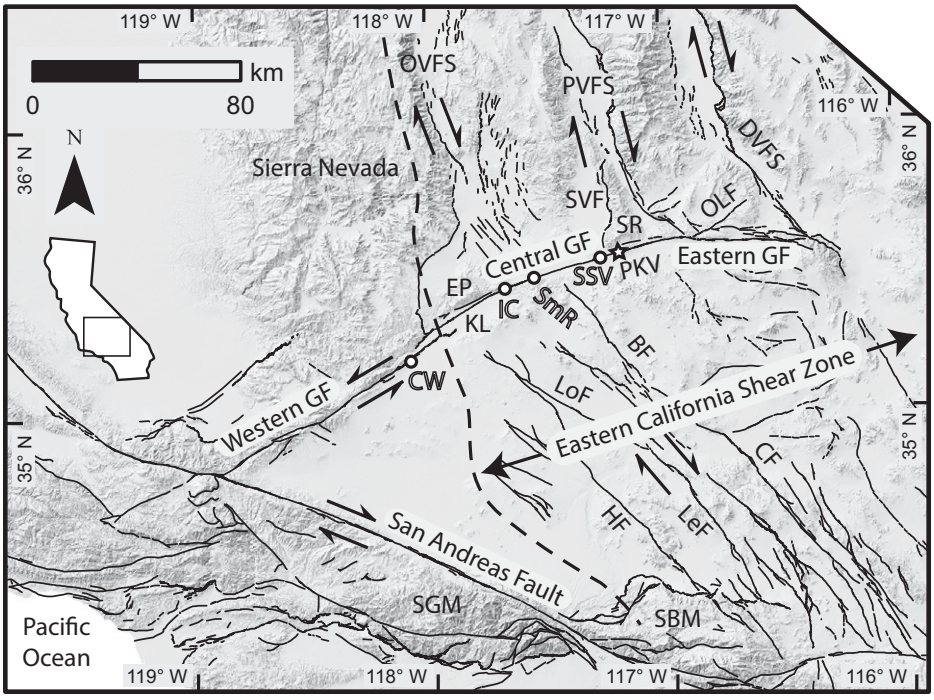


**Figure 1. Shaded-relief topography and Quaternary fault map (Quaternary fault and fold database for the United States, U.S. Geological Survey and California Geological Survey, 2006) of southern California. Inset map of California with rectangular box locates image. Arrows indicate sense of strike-slip motion. White star shows location of offset late Holocene alluvial fan deposit (this study). White circles show locations of existing Garlock fault (GF) slip-rate and paleoseismic studies: CW—Clark Wash (McGill et al., 2009); IC—Iron Canyon (McGill and Rockwell, 1998 and Dawson et al., 2003); SmR—Summit Range (Ganev et al., 2012); SSV—Southeast Searles Valley (McGill and Sieh, 1993). Heavy dashed line locates the western margin of the Eastern California shear zone. BF—Blackwater fault; CF—Calico fault; DVFS—Death Valley fault system; EP—El Paso Mountains; HF—Helendale fault; KL—Koehn Lake; LeF—Lenwood fault; LoF—Lockhart fault; OLF—Owl Lake fault; OVFS—Owens Valley fault system; PKV—Pilot Knob Valley; PVFS—Panamint Valley fault system; SBM—San Bernardino Mountains; SGM—San Gabriel Mountains; SR—Slate Range; SVF—Searles Valley fault.**

Although the Eastern California shear zone accommodates ~10–14 mm/yr of right-lateral shear (Bennett et al., 2003), the nature of the interaction between right-lateral fault systems in eastern California and left-lateral slip along the Garlock fault remains enigmatic. Fault systems of the Eastern California shear zone terminate both north and south of the Garlock (Oskin and Iriondo, 2004; Numelin et al., 2007) and do not appear to significantly disrupt the western and central segments of the fault zone (e.g., McGill and Sieh, 1991).

Despite the apparent continuity of the Garlock fault, dextral shear associated with the Eastern California shear zone clearly passes across the fault along a NNW-trending zone (Savage et al., 1990; Bennett et al., 2003; Miller et al., 2001). Dextral shear could be accommodated by progressive rotation of the Garlock fault (Savage et al., 2001; Gan et al., 2003; Savage et al., 2004), or it may be accommodated by oscillatory strain release along different segments of the conjugate fault network (Peltzer et al., 2001). The latter hypothesis finds support in paleoseismic records (Rockwell et al., 2000), which reveal that Eastern California shear zone faults slip in clusters that appear to be anti-phased with respect to paleoseismic records from the Los Angeles basin (Dolan et al., 2007). Understanding the nature of interaction among the Eastern California shear zone, the Garlock fault and the San Andreas system is thus a key goal of developing refined slip histories along each of these systems.

The Garlock fault exhibits along-strike variations in fault orientation and slip-rate (e.g., McGill and Sieh, 1993; McGill et al., 2009). Western segments of the fault system appear to have higher rates of slip, with rates decreasing to near zero at the eastern fault termination (Meade and Hager, 2005). Along the central segment, displacements of the highstand shoreline of Searles Lake provides one of the most robust determinations of displacement since Late Pleistocene time (82–106 m, preferred estimate of ~90m; McGill and Sieh, 1993). Lacustrine records from Searles Valley suggest that lake recession from highstand conditions occurred near 15–16 ka (Lin et al., 1998), and thus, average slip rates along the central Garlock fault are 5–7 mm/yr. Displaced alluvial fans along the flank of the Summit Range (~70 m in 12–19 k.y., Ganev et al., 2012) suggest similar rates of ~4–7 mm/yr. Slip rates along the western Garlock fault may be somewhat higher at ~5–11 mm/yr (McGill et al., 2009), although a constant rate from Clark Wash to Searles Valley cannot be ruled out.

Paleoseismic studies along the Garlock fault provide additional constraints on the behavior of the fault system over the past ~7 k.y.. Along the central fault segment (Fig. 1), trench records reveal 6 well-resolved events since ~7 ka (McGill and Rockwell, 1998; Dawson et al., 2003). Notably, four of these events occurred during the past 2 k.y.; these were preceded by a period of apparent quiescence during the period between ~5–2 ka (Dawson et al., 2003). Presuming that these events record similar surface displacement (McGill and Sieh, 1991), this record of paleoearthquakes suggests the possibility of irregular slip histories for nearby sections of the Garlock fault.

## STUDY AREA

In an effort to test the possibility of time-variant slip rates along the Garlock fault, we identified displaced alluvial deposits and surfaces in Pilot Knob Valley, ~6 km east of the displaced Searles Lake shoreline documented by McGill and Sieh (1993). Our site is located at 117° 12′ 7″ W, 35° 33′ 36″ N, where three small drainages cross the Garlock fault (Fig. 2A and B) and are incised into Quaternary alluvial and lacustrine deposits along the southern flank of the Slate Range. The western and eastern channels are active and are labeled $W_a$ and $E_a$, respectively, on Figure 2. A presently abandoned channel $W_i$, branches off $W_a$ upstream of the fault; this drainage contains an extensive deposit of late Holocene alluvial material (labeled $Qa3_b$ in Figure 2C, Table 1). These deposits are truncated to the south by the Garlock fault, along which slip has juxtaposed a shutter ridge composed of relict alluvial fan material (labeled Qa5 in Figure 2C, Table 1) against the Qa3 material.

The $Qa3_b$ deposit displays geomorphic and sedimentologic characteristics consistent with high-energy transport in a confined alluvial fan environment. These include: (1) original bar and swale surfaces with relief up to ~1 m; (2) abundant clasts >25 cm in diameter; (3) poorly graded and sorted beds 5–25 cm thick, comprising a generally matrix-supported coarse sand and gravel, and a lesser abundant clast-supported cobble and boulder alluvium; and (4) stacked parallel

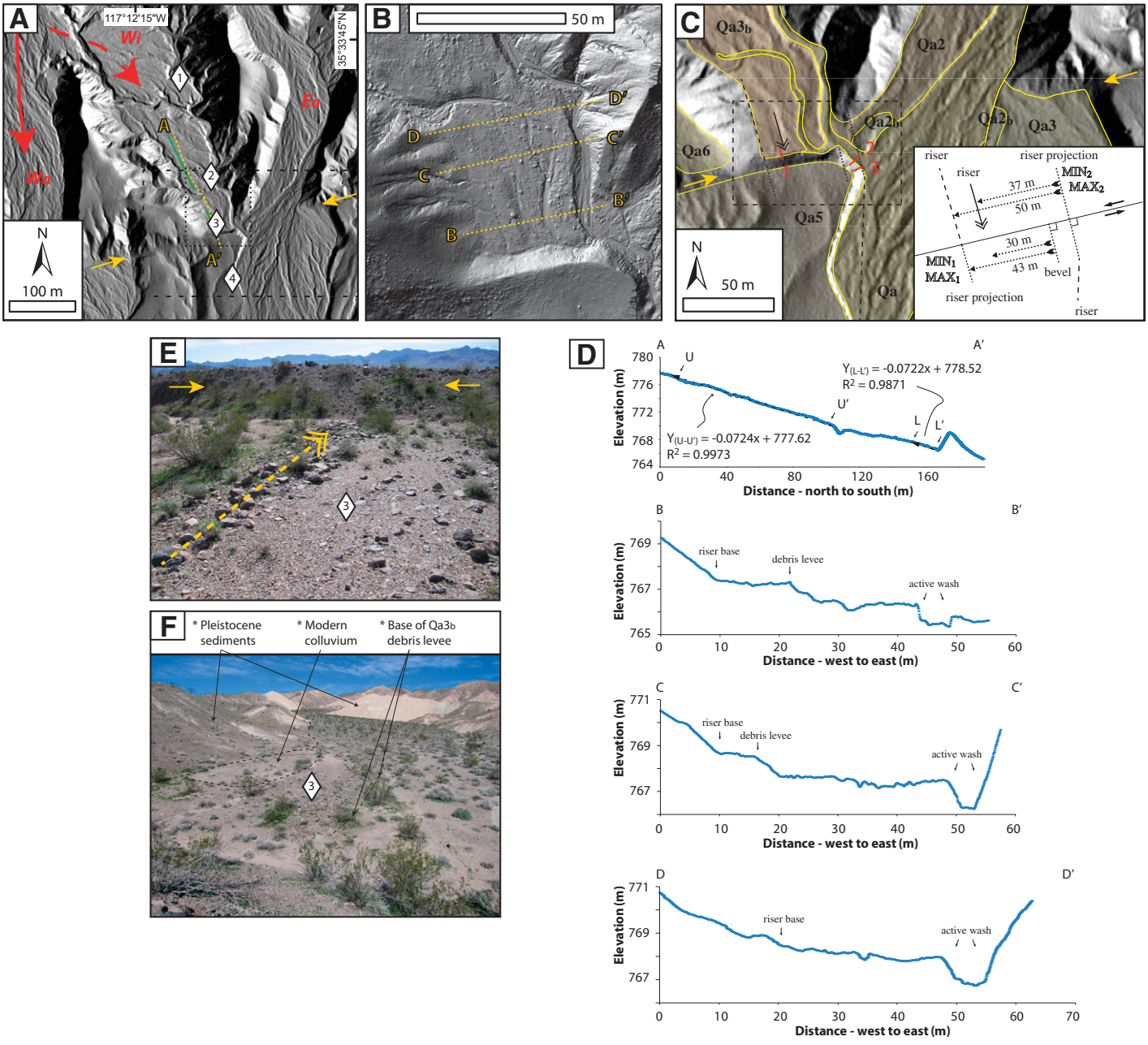


**Figure 2. (A) A 0.5-m-resolution Earthscope LiDAR hillshade image of the study area in northern Pilot Knob Valley. Small yellow arrows locate the Garlock fault. Red arrows indicate sediment transport direction for the modern (solid line) and abandoned (dashed line) stream channels. $W_a$ and $W_i$ are the active and inactive western channels, respectively, and $E_a$ is the active eastern channel. Surfaces and deposits at the northern end of the abandoned channel are commensurate in composition, morphology and age with those close to the shutter ridge, suggesting channel abandonment 3.5-4.5 ka. White diamonds indicate: (1) OSL-PVK-2 OSL sample site (Fig. 4 & data repository), (2 & 3) soil profile sites CLK-2 and CLK-1 (Table 2), respectively, and (4) TCN-PKV-2 $^{10}$Be cosmogenic profile site (Fig. 5). The smaller, finely dotted box shows location of Figure 2B. The larger, coarsely dashed rectangle shows location of Figure 2C. Dashed yellow line (A-A′) locates the downstream elevation profile shown in Figure 2D. Solid neon green lines represent U-U′ and L-L′ segments of the A-A′ profile in Figure 2D. (B) A 5-cm-resolution terrestrial LiDAR hillshade image of the southern termination of channel $W_i$. Dashed yellow lines (B-B′, C-C′ and D-D′) locate the cross-stream elevation profiles shown in Figure 2D. (C) Close-up Earthscope LiDAR hillshade image of offset channel with inset box highlighting offset interpretations. Dotted box shows location of inset box. Red lines and numbers indicate hand-dug trench locations (Fig. 3). (D) Elevation profile A-A′ (dashed yellow line in Figure 2A) comprises segments U-U′ and L-L′ (neon green solid lines) of the upstream debris flow intersecting the north-facing shutter ridge. Here, a consistent slope suggests that no ponding of sediments occurred that would result in a decreased slope of L-L′ relative to U-U′. Profiles B-B′, C-C′ and D-D′ (dashed yellow lines in Figure 2B) shows the elevation across the $W_i$ channel surface and shows position of an active wash that is most likely responsible for the beveled eastern shutter ridge. (E) Southward-looking field photo of debris levee (dashed double-headed dark yellow arrow) that is oriented nearly orthogonal to the shutter ridge. (F) Northward-looking field photo of debris levee and channel $W_i$ from the perspective of the top of the shutter ridge.**

TABLE 1. UNIT DESCRIPTIONS FOR PILOT KNOB VALLEY SITE

| Unit Label | Age Estimate (ka) | Description |
|---|---|---|
| Qa | 0 – 0.1 | Modern wash – no degradation of surface, excellent bar and swale features inside oftentimes incised channels, largely devoid of vegetation |
| Qa2 | 0.1 – 0.5 | Not cut by last earthquake rupture, incipient bushes and grasses, incised by active channels, otherwise similar morphology to Qa |
| $Qa2_b$ | 0.5 – 1 | Cut by most recent earthquake rupture, otherwise similar to Qa2 |
| Qa3 | 1 – 3 | Well-preserved bar and swale, incipient pavement development on flat surfaces, no varnish on tops of clasts or rubification on bottoms of clasts, no discernable soil development other than ~0.5-1 cm thick Av-horizon |
| $Qa3_b$ | 3.5 – 4.5 | Well-preserved bar and swale, minimal pavement development on flat surfaces, incipient varnish on tops of clasts in cavities, minor rubification on clasts bottoms, incipient soil development (stage I carbonate) with 1–2 cm thick Av-horizon |
| Qa5 | 15 – 40 | Good pavement development, clasts touching, clasts are varnish & rubified, sparse vegetation, 5+ cm thick AV-horizon with 20–30 cm thick Bt-horizon, stage II-III carbonate soil, incised several meters locally |
| Qa6 | 40 – 60 | Strong pavement development, clasts touching, clasts are varnished & rubified, sparse vegetation, 7–10 cm thick AV-horizon with 20–30 cm thick Bt-horizon, stage III carbonate soil, incised 10+ m locally |

and trough-cross bedding, interpreted to be sheet flood and braided stream deposits, respectively. Silt lenses and mud drapes on bedding planes are locally present, but volumetrically rare. The slope of the deposit is relatively uniform at ~4° along length of $W_i$ channel (Fig. 2A and D).

Several linear arrangements of boulder bar comprise a prominent channel levee atop the $Qa3_b$ surface (Fig. 2). This north-south levee is composed of an open-framework cluster of boulders ranging from 25 to 50 cm in diameter and can be traced to within 2 m of the shutter ridge along the Garlock fault (Fig. 2). East of this feature, the $Qa3_b$ surface is dissected by two active gullies that have incised 0.5–1 m into the deposit (Fig. 2B and D); both gullies deflect in a right-hand sense as they approach the shutter ridge (Fig. 2). Although the boulder levee appears to separate two levels of the $Qa3_b$ deposit, separated by ~50–80 cm elevation (Fig. 2D), we do interpret this feature as a terrace riser separating diachronous surfaces. We observe no difference in the characteristics of the surface clasts, their degree of varnish or rubification, on either side of the levee, and the degree of bar/swale development is similar on the $Qa3_b$ surface on either side of this feature (Fig. 2E and F). Moreover, topographic profiles extracted from high-resolution LiDAR (light detection and ranging) topographic data show (Fig. 2B) that the $Qa3_b$ topographic surface is in fact continuous across the levee at its northern end; there is no topographic step that might represent a terrace riser (Fig. 2D). Thus, although the $Qa3_b$ deposit has been subtly eroded by modern gullies east of the boulder levee, we do not see strong evidence for an inset terrace that might indicate diachroneity of surface development north of the fault (e.g., Cowgill, 2007).

The shutter ridge south of the Garlock fault is 50 m in length, measured from western wall of channel $W_i$ north of the fault to the western tip of channel $E_a$ south of the fault (Fig. 2C). The shutter ridge is composed of alluvial fan gravels with a significant component of felsic and intermediate intrusive igneous clasts, and lesser meta-sedimentary and meta-igneous clasts, derived from the southern Slate Range; thus, the material is relatively short traveled and comparable to modern sediment in the active wash. The northeastern corner of the shutter ridge is rounded and appears to have been subjected to lateral erosion by the modern gully (Fig. 2). Projection of the straight margin of the shutter ridge northward to the Garlock fault suggests that at least 7 m has been removed (Fig. 2); this value is a minimum, as we cannot determine how much lateral erosion has occurred away from the fault.

To address stratigraphic and tectonic relationships between the $Qa3_b$ deposit and the shutter ridge, we hand-excavated three trenches at key locations. Trench 1 is a 6.75-m-long trench immediately west of the boulder levee on the $Qa3_b$ surface (Fig. 3). We identified four stratigraphic units and one pedogenic unit; Qsa was identified as a bioturbated zone with an incipient Av soil horizon displaying a vesicular matrix texture of fine, eolian silt beneath a pavement surface of clasts. Beneath this, a continuous wedge of colluvial material (Qc2) extends northward ~3.5 m from the shutter ridge and extends across underlying alluvial deposits. Qc2 is distinguished from underlying alluvial units by its (1) lack of bedding and sorting, (2) higher eolian silt content and associated light gray-tan color and (3) higher porosity and vesicular texture. Beneath Qc2, alluvium that is continuous with the $Qa3_b$ deposit comprises two coarse sand and gravel conglomeratic facies, Qd1 and Qd2. These two sub-facies exhibit scoured bases and imbricated clasts indicating southward paleoflow. Moreover, they exhibit weak soil development consistent with our two $Qa3_b$ soil profile descriptions (see following section). Qd1 was not observed interfingering with colluvium, which might be expected if the shutter ridge were present during $Qa3_b$ deposition. A third unit, Qd3, is exposed at the bottom of the trench and appears to be distinct from Qd1and Qd2 in that it is noticeably more indurated and rubified, with stage III petrocalcic horizons permeating the sandy matrix. We interpret this as an older deposit that predates emplacement of $Qa3_b$.

Trenches 2 and 3 were excavated south of the Garlock fault across the eroded northeastern corner of the shutter ridge to ascertain whether material related to $Qa3_b$ was present. Both trenches were dug to 1–2 m depth and penetrated the underlying shutter ridge material (Qd4 in Fig. 3). Excavation did not reveal the presence of Qd1, Qd2, or Qd3 material here. Rather, we observe deposits (Qda) that appear continuous with young (late Holocene?) mapped as Qa2 in Figure 2. Qda is shown to be younger than Qd1 based on two relationships: (1) a lack of observable pedogenetic characteristics in the exposed Qda deposit and (2) continuity of Qda with deposits composing Qa2 surfaces. The absence of relic $Qa3_b$ deposits within these two trenches suggests that the shutter ridge was most likely eroded post-$Qa3_b$ deposition. However, we cannot rule out that some lateral erosion of the shutter ridge occurred prior to $Qa3_b$ scouring and deposition.

## LATE HOLOCENE DISPLACEMENT

The geologic relationships described above allow us to place bounds on the magnitude of displacement subsequent to deposition of $Qa3_b$. We consider two end-member possibilities, the difference between which depends on whether the full 50 m extent of the shutter ridge was emplaced after deposition (MAX estimates, Fig. 2C) or whether some length of shutter ridge was present during deposition (MIN estimates, Fig. 2C). We consider each below.

The most conservative scenario considers that an ~13 m long shutter ridge was present during deposition of $Qa3_b$ (Fig. 2C); this reconstruction places the eastern edge of the shutter ridge in line with the boulder levee atop $Qa3_b$. If we assume that the inside corner of the beveled eastern shutter ridge was aligned with the boulder levee, we reconstruct a minimum displacement of 30 m ($MIN_1$, Fig. 2C). However,

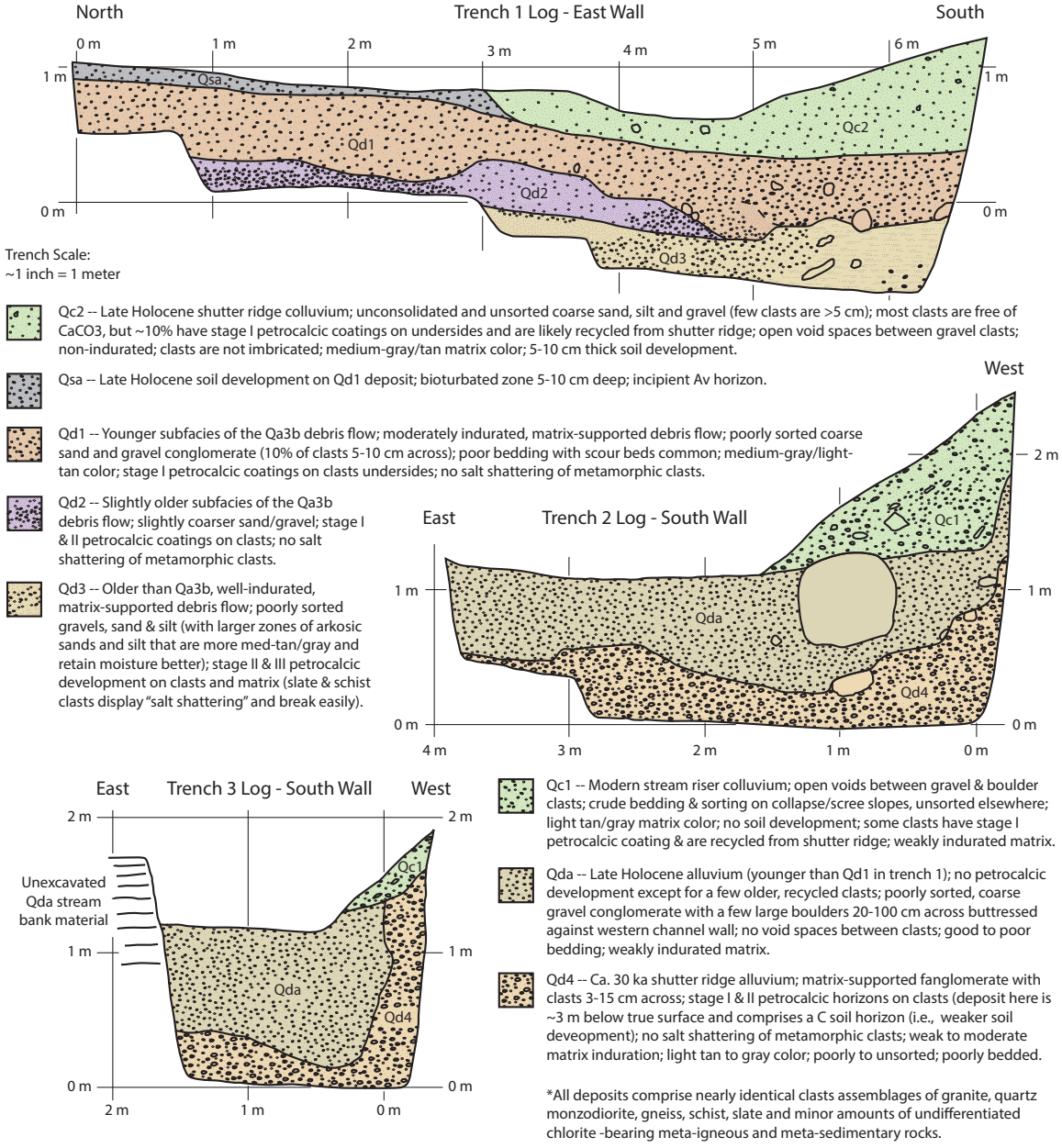


**Figure 3. Trench logs illustrating sedimentologic relations along the north face of the shutter ridge (A) and the northeast, beveled corner (B and C). See Figure 2 for locations. $Qa3_b$ deposit lies beneath shutter ridge colluvium (trench 1) and is not present in trenches 2 and 3.**

as argued above, it appears that lateral erosion of the shutter ridge post-dates $Qa3_b$ deposition and thus we require an additional 7 m of displacement ($MIN_2$, Fig. 2C). It is important to note that these minimum scenarios implicitly assume that the $Qa3_b$ surface is diachronous and somewhat older to the west of the boulder levee (Fig. 2).

Deposition of $Qa3_b$ is interpreted to predate most, if not all, of the present-day width of the shutter ridge. Five lines of evidence support this interpretation. First, original bar and swale surfaces that represent the paleo-flow directions during fan deposition are aligned perpendicular to the shutter ridge (Fig. 2E and F). We observe no deflection of bar and swale features around the eastern extent of the shutter ridge, as would be expected if the shutter ridge were present during deposition (e.g., Cowgill, 2007). Second, we observe no decrease in fan slope that would indicate ponding of sediments north of the shutter ridge (Fig. 2D, profile A-A′) during development of a backwater reach upstream of the shutter ridge. Third, the relief between bar and swale is up to ~1 m and bars contain abundant clasts >10 cm in diameter, features associated with deposition during vigorous channel flow. Thus, the grain size of the deposits does not appear to fine toward the fault, as would be expected if the shutter ridge had formed a barrier to flow. Fourth, the $Qa3_b$ deposit appears to be a single depositional surface. There is no older alluvial deposit along the western edge of channel $W_i$ immediately north of the fault, as might be expected if the shutter ridge was present prior to $Qa3_b$ deposition (Fig. 2D, profile B-B′). Finally, hand excavation reveals that the $Qa3_b$ deposit projects beneath the collu-

vial apron developed along the northern scarp of the shutter ridge for at least 3.5 m (Fig. 3), suggesting that erosion of the scarp post-dates $Qa3_b$ deposition. We found no evidence to suggest that the shutter ridge colluvium consists of stacked or discrete prograding colluvial wedges, nor do we see any indication that the colluvial wedge exposed interfingers with $Qa3_b$. In contrast, the absence of $Qa3_b$ material beneath the active wash along the northeastern corner of the shutter ridge suggests recent erosion of the shutter ridge. Collectively, these observations indicate that the $Qa3_b$ deposit likely filled the entire width of the valley and does not represent a younger inset surface or a diachronous tread (e.g., Cowgill, 2007). Thus, it seems apparent that displacement of the shutter ridge truncated $Qa3_b$ deposits.

Considering these arguments, the maximum displacement implied by our data is that the shutter ridge did not protrude into channel $W_i$ during $Qa3_b$ deposition (referred to as $MAX_1$ and $MAX_2$ displacements in Fig. 2C inset). In this case, the eastern end of the shutter ridge is restored to match the channel wall north of the Garlock fault, implying ~43 m of displacement ($MAX_1$, Fig. 2C). If we account for lateral erosion of the shutter ridge, this estimate may be as high as 50 m ($MAX_2$, Fig. 2C).

Lateral erosion of the downstream riser in channel $E_a$ is accounted for in both the minimum and maximum displacement scenarios (Fig. 2C). The absence of $Qa3_b$ material beneath the active wash along the eroded northeastern corner of the shutter ridge makes it seem likely that most erosion of the shutter ridge postdates deposition of $Qa3_b$. Thus, we prefer scenarios that account for this additional 7 m of displacement ($MAX_2$ and $MIN_2$, Fig. 2C). Moreover, as argued above, we do not see strong evidence for diachroneity of the $Qa3_b$ surface in the topography, morphology of the surface, or soil characteristics, and therefore we prefer the maximum reconstruction of 43–50 m. Of course, we cannot rule out the possibility that lateral erosion of the shutter ridge exceeded 7 m, and it is possible that displacement subsequent to deposition of $Qa3_b$ may exceed 50 m. However, we note that apparent offset of the eastern $E_a$ channel wall is ~47 m (e.g., Helms et al., 2003), consistent with our preferred maximum restoration. Thus, we find it likely that the width of the shutter ridge represents most of the displacement that has accrued along the central Garlock fault since deposition of $Qa3_b$.

## ALLUVIAL CHRONOLOGY

To evaluate the age of the $Qa3_b$ surface, we employed two techniques; the relative degree of soil development and direct dating of the burial of fine-grained silt lenses within the deposit. The pronounced bar-and-swale depositional morphology of the $Qa3_b$ surface and weak development of soil and desert pavement (Table1) indicate that this is a relatively young deposit (e.g., Bull, 1991; Helms et al., 2003, McDonald et al., 2003). The relative degree of soil developed on the $Qa3_b$ deposit when compared to several independently dated soils in the southwest United States (Table 2) indicates the $Qa3_b$ deposit is late Holocene. The degree of soil development characterized on the $Qa3_b$ deposit (soils CLK-1, CLK-2; Table 2) is strongly similar to soils formed in several Late Holocene deposits developed in generally similar parent materials (i.e., alluvium derived from largely siliceous intrusive plutonic and metamorphic source rocks) and broadly under similar climatic conditions (i.e., arid climate with annual precipitation from ~100–150 mm/yr). Although there are small differences in seasonality of precipitation between the MM soil and the other soils have formed in the Mojave Desert, we consider these to be minor influences (Table 2).

Common characteristics of Late Holocene soils shown in Table 2 include a weak to moderately developed Av (vesicular) horizon, weakly developed Bwk (see Table 2 for nomenclature) or Bky horizons, and stage I carbonate morphology (e.g., Machette, 1985). The CLK-1, CLK-2, MM, PM Qf6, and SIL-1 soils that have formed on gravelly to cobbly alluvial deposits have weakly development desert pavements, whereas the CWG-2 soil that has formed on gravelly sand deposits does not have a pavement. By comparison, soils formed on alluvial deposits that are pre-late Holocene and older than ca. 8 ka (generally on early Holocene to Latest Pleistocene deposits) have moderately to strongly developed Av horizons, weakly to moderately developed Bwk, Btk, Bky and Bty horizons, and stage I-III carbonate morphology. Desert pavements are moderately to strongly developed on the PM Qf5 and CLK-3 soils that have formed in gravelly to cobbly alluvial deposits and do not exists on the CWG-1 soil that has formed in gravelly sand alluvium.

Soil morphology was quantified using the Soil Development Index (SDI) procedure according to Harden (1982), Harden and Taylor (1983) and Birkeland (1999). The SDI provides a semi-quantitative approach to convert field-described soil morphology (i.e., color, structure, texture) into numerical data to enable a quantitative comparison of the degree of soil development. Morphologic values can be calculated for up to ten morphologic parameters for each soil horizon including: rubification (reddening), color paling, color lightening, melanization (darkening), total texture, dry consistence, moist consistence, argillans (clay films), structure, pH and carbonate morphology. In this study we applied morphologic values for rubification (reddening), total texture, dry consistence, moist consistence, argillans and structure, as these six values best represent time-related trends in formation for the soils used here. Points are assigned to each property based on the difference between the described soil property and the parent material (i.e. the morphologic nature of the deposit at the onset of soil formation). Points for each property are normalized to a percentage scale of maximum property development based on comparison of each property to a published or conceptual maximum value of development for each particular property. Maximum soil property values from Taylor (1988) were used to normalize soil property values in this study. Normalized property values are summed for each horizon and averaged yielding a Horizon Development Index (HDI) value that provides an estimate of overall horizon development relative to a conceptual idea of maximum possible horizon development. HDI values are multiplied by horizon thickness and summed for each profile yielding a single Profile Development Index (PDI) value for that profile (note: the SDI is used to convert soil morphology into a final PDI soil value). PDI values provide a means of comparison among soils within a given sequence and can be used to develop a soil chronofunction.

The chronofunction can be inverted to provide soil age estimates based on calculated PDI values. Increasing PDI values reflect an overall increasing development of soil profile morphology that is largely reflective of increasing soil age. The PDI values for soils formed on dated Late Holocene deposits (MM, PM Qf6, CWG-2, and SIL-1; Table 2) range from 2.5 to 4.2 and overlap the PDI values of 3.1 and 3.6 for soils formed on the $Qa3_b$ deposit (CLK-1, CLK-2). The PDI values for the soils on the three pre-Holocene deposits are higher and range from 7.9 to 44.1, reflecting the longer time for soil development that has occurred on these older surfaces. The fact that PDI values for the two soils formed on the $Qa3_b$ deposit are lower than PDI values from dated pre-Holocene surfaces and similar to PDI values from dated late Holocene surfaces supports that that the $Qa3_b$ deposit is younger than ca. 4.5 ka.

To test this inference, we collected fine-grained sand and silt from a lens within the $Qa3_b$ deposit (Fig. 2A) for optically stimulated luminescence (OSL) dating (OSL-PKV-2 in Fig. 4). We sampled a freshly exposed silt interval ~1.1 m below the $Qa3_b$ tread surface, and ~1.5 m above the modern stream bed, filling four 6 by 22 cm stainless steel cylinders. Samples were

TABLE 2. MOJAVE SOILS PROFILE DEVELOPMENT INDEX (PDI) CHRONOFUNCTION FOR ALLUVIAL FAN DEPOSITS

| Site | General horizon sequence[1] | Carbonate stage[2] | Pavement development | PDI value[3] | Numerical age (ka)[4] | Location (UTM) | Reference |
|---|---|---|---|---|---|---|---|
| Soils formed on Late Holocene alluvial deposits | | | | | | | |
| CLK-1 | Av-Bwk-Bky-Cky | I | Weak | 3.1 | 3.7-4.5* | 11S 481623 3935177 | This study[6] |
| CLK-2 | Av-Bwk-Bky-Cky | I | Weak | 3.6 | 3.7-4.5* | 11S 481606 3935311 | This study[7] |
| MM[5] | Avk-Bwk-Ck-Cky | I | Weak | 2.5 | 2.9-3.2** | 11S 761465 3635878 | Bacon et al (2010) |
| PM Qf6 | Avk-Bwk-Ck-C | I | Weak | 4.2 | 3.5-4.2*** | 11S 623901 3896382 | McDonald et al (2003) |
| CWG-2 | A-C-Ab1-Ckb1-Ab2-Ckb2-Cb2 | I- | Weak | 2.2 | 2.3-2.7** | 11S 401126 3896325 | McGill (2009)—Soil formed in deposit Hya |
| SIL-1 | Av-Bwk-Ck-C | I | Weak | 1.8 | 2.9-3.6* | 11S 580056 3929066 | Mahan et al (2007)—Site M999VJ-991 |
| Soils formed on pre-Late Holocene alluvial deposits | | | | | | | |
| CWG-1 | A-AB-Bwk-CBk | I-II | Weak-moderate | 7.9 | 7.6-8.1** | 11S 401140 3896382 | McGill (2009)—Soil formed in deposit Hoc |
| PM Qf5 | Avk-Bwk-Btk-Ck-C | II | Moderate-strong | 12.1 | 8.4-14.1*** | 11S 624155 3862427 | McDonald et al (2003) |
| CLK-3 | Av-Btk-Bty-Bky-CBky-Cky | II-III | Strong | 44.4 | 21.6-31.9**** | 11S 481646 3935102 | This study[8] |

[1]Horizon nomenclature: k (pedogenic carbonate), t (translocated clay and silt), w (incipient color or structure development), y (pedogenic gypsum).
[2]Carbonate morphologic stage (Gile et al., 1981).
[3]Profile Development Index (PDI). Soil morphology was quantified using the Soil Development Index (SDI) procedure according to Harden (1982), Harden and Taylor (1983), Taylor (1988) and Birkeland (1999).
[4]Quantitatively determined age using the following dating techniques: *Optically stimulated luminescence (OSL), **Radiocarbon dating of wood fragment, *** Infrared stimulated luminescence (IRSL), ****Depth profile using $Be^{10}$.
[5]The MM soil has formed under a modern climate that has rainfall derived from both winter frontal and summer convective storms whereas all other soils listed in Table 2 have formed in the Mojave Desert where rainfall is primarily derived from winter frontal storms and secondarily from summer convective storms.
[6]White diamond "3" on Figure 2A. See Figure 4 and Table 3 for OSL analytical data corresponding to CLK-1 pit.
[7]White diamond "2" on Figure 2A.
[8]White diamond "4" on Figure 2A. See Figure 5 and Table 4 for $^{10}Be$ analytical data corresponding to TCN-PKV-2 and CLK-3 profiles.

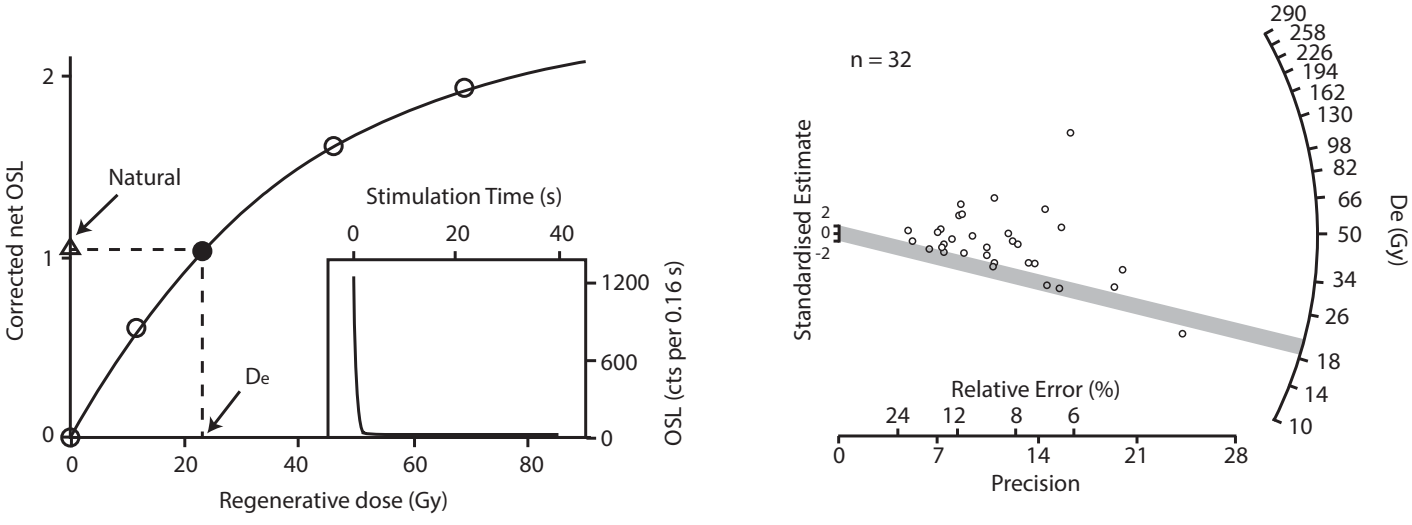


**Figure 4. Optically stimulated luminescence plots for sample OSL-PKV-2. Sample was collected from a $Qa3_b$ silt lens (see Fig. 2A for location) at 1.1 m vertical depth on a freshly incised ~2.5-m-high stream bank. A calibration growth curve (above left) illustrates the typical sensitivity corrected luminescence signal as a function of laboratory-induced regenerative dose (Gy) for a single aliquot. The filled circle is luminescence data for a repeated regenerative dose at the end of the measurement cycle; a value of unity in the ratio of these replicated measurements indicates correction of any luminescence sensitivity change throughout a measurement sequence. The equivalent dose, $D_e$ is found by interpolation of the natural luminescence signal with the regenerative-dose growth curve. An inset decay signal plot reveals a strong ~1200 initial count with a fast decay when exposed to a blue diode light source, indicative of good quartz sensitivity. The radial plot (above right) shows the $D_e$ in values of grays (e.g., Galbraith, 1990), for 32 aliquots, as a function of its relative error and precision. Samples plotting to the right are more precise and have lower relative error. $D_e$ is the effective amount of environmental radiation received since bleaching and deposition. The shaded bar on radial plot fits a 2σ uncertainty space through the five aliquots, comprising the minimum age model, to estimate a representative $D_e$ for the sample. A minimum age model is appropriate here (Galbraith et al., 1999) because of the over dispersion and asymmetrical population of $D_e$ values measured (~61%), characteristic of incomplete bleaching of quartz grains during transport. An aliquot plotting below this bar is treated as an outlier, and thus not used to determine a bulk $D_e$ for OSL-PKV-2. Table 3 in the text gives a separate summary of the dating information. Data Repository item DR1 (see footnote 1) provides summary of methodology used.**

TABLE 3. OPTICALLY STIMULATED LUMINESCENCE (OSL) DATING SUMMARY FOR LATE HOLOCENE ALLUVIAL DEPOSIT

| $D_e$[1] (Gy) | $^{234}Th$[2] (Bq.kg$^{-1}$) | $^{226}Ra$[3] (Bq.kg$^{-1}$) | $^{228}Ra$[4] (Bq.kg$^{-1}$) | $^{40}K$ (Bq.kg$^{-1}$) | $W_{in\text{-}situ}$ (%) | Cosmic[5] (mGya$^{-1}$) | Total dose-rate (mGya$^{-1}$) | OSL age (ka) |
|---|---|---|---|---|---|---|---|---|
| 19.81 ± 1.55 | 43.8 ± 14.2 | 32.4 ± 1.49 | 45.8 ± 1.97 | 1092.5 ± 5.46 | 0.68 | 0.21 | 4.87 ± 0.23 | 4.07 ± 0.37 |

[1]Equivalent dose—calculated using Minimum Age Model.
[2]Average of $^{234}Th$ at 63 and 93 keV.
[3]Average of $^{226}Ra$ at 186 keV and 6 further gammas in decay series.
[4]Average of $^{228}Ra$ and 5 further gammas in decay series.
[5]Uncertainty 10%.

analyzed at Kansas State University (see GSA Data Repository[1]).

This sample displayed luminescence characteristics consistent with young, partially bleached alluvial sediments and yielded an age of 4.07 ± 0.37 ka (Fig. 4, Table 3), consistent with the pedogenic and geomorphic characteristics of the deposit. Its measured decay signal reveals a strong initial count with a fast decay when exposed to a blue diode light source, indicative of robust quartz sensitivity. A minimum age model (Galbraith et al., 1999) is considered appropriate because of the over dispersion and asymmetrical population of $D_e$ (equivalent dose) values (Fig. 4) measured (~61%), characteristic of incomplete bleaching of quartz grains during transport. A complete discussion of luminescence behavior and interpretation can be found in the Data Repository (DR1; see footnote 1). In conjunction with the degree of soil development, these results suggest that deposition of unit $Qa3_b$ occurred in the Late Holocene, between 3.5–4.5 ka (Table 3).

We also dated the older Qa5 alluvial fan surface which comprises the shutter ridge south of the Garlock fault (Fig. 2A) by measuring a depth profile of $^{10}Be$ nuclide concentration (Fig. 5, Table 4). The soil profile at this site exhibits significant rubification, accumulation of clays, and development of moderate pedogenic carbonate relative to the Holocene deposits (Table 2). Five samples were collected from a vertical stream bank cut into the alluvial fan (TCN-PKV-2 in Table 4), and a single surface sample was amalgamated from clasts ~1–3 cm diameter. Samples were washed, sieved to retain the 250–500 µm sediments, and chemically and physically abraded to concentrate quartz; Be was isolated via anion and cation chromatography, and converted to Be-oxide at the University of Kansas. Final $^{10}Be$ concentration analysis was performed on an accelerated mass spectrometer (AMS) at Purdue University (PRIME Lab). Best-fit profiles utilizing 100,000 Monte Carlo simulations using the "10Be_profile_simulator_V1.2" script of Hidy et al., [2010], that consider local production and the possibility of surface erosion/inflation. Best-fit models that allow for some surface inflation (i.e., incorporation of windblown material into the Av horizon and uppermost B horizon) suggest that the alluvial fan is ca. 30 ka in age (25.8 +6.1/-4.2 ka at 2σ) (Fig. 5, Table 4), consistent with the greater degree of soil development on the fan surface (CLK-3 in Table 2).

## TECTONIC SIGNIFICANCE

Our results demonstrate that at least 30 m, and up to 50 m, of sinistral displacement has accumulated along the central Garlock fault in Pilot Knob Valley since 3.5–4.5 ka. These data require that average slip rates during the late Holocene were between 6.7 and 14.3 mm/yr, significantly greater than average rates determined from Late Pleistocene features (e.g., McGill and Sieh, 1993; Ganev et al., 2012). If we consider a central $Qa3_b$ age of 4 ka and our preferred displacement range of 43–50 m, our data imply that the average slip rate along the Garlock fault was 10.8–12.5 mm/yr during the Late Holocene (Fig. 6).

These results provide important new temporal resolution of the history of strain release along the central Garlock fault. Displacement of the Searles Valley shoreline by ~90 m is well constrained near Randsburg Wash ~6 km west of our study (McGill and Sieh, 1993); this appears to be consistent with 70 ± 7 m offsets documented along the nearby Summit Range to the west (Ganev et al., 2012). Assuming no spatial variations in slip rate across the 6 km that separate our site from the displaced shoreline, our results require that 43–50 m of this displacement accrued in the past ~4 k.y. The remaining 40–47 m must have accrued in the interval of time between ca. 15 ka (the age of the Searles Valley shoreline) and 4 ka. The interval slip rates implied by these data suggest relatively slow displacement (~3.6–4.3 mm/yr) during this time (Fig. 6). Although the extreme minimum slip rate allowed by our data is close to the maximum average rate inferred from the Searles Valley shoreline (McGill and Sieh, 1993), the separation between the interval rates (Fig. 6) strongly suggests that slip rates have varied through time. Thus, our results provide the first confirmation of previous inferences of time-variant strain accumulation and release along the Garlock fault (Peltzer et al., 2001; Chuang and Johnson, 2011; Ganev et al., 2012).

Interestingly, our results appear to find support in the Late Holocene paleoseismic record and surficial offsets from the central Garlock fault (e.g., McGill and Sieh, 1991; Dawson et al., 2003). Analysis of clustered displacements

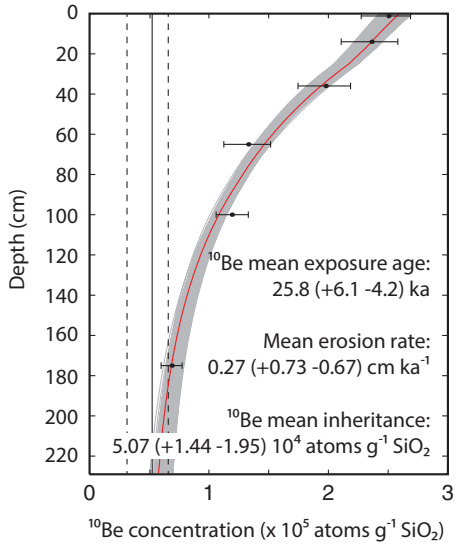


**Figure 5. Plot of sample depth versus $^{10}Be$ concentration for profile TCN-PKV-2 from a displaced alluvial fan south of the Garlock fault at 35° 33′ 50″ N, –117° 12′ 09″ W and 792 m above sea level in Figure 2. Gray region represents 3σ solution space for 100,000 Monte Carlo regression simulations fit through all surface and depth samples (solid black circles) using the Matlab-based "10Be_profile_simulator_V1.2" script of Hidy et al., (2010). Error bars represent 2σ total $^{10}Be$ concentration measurement uncertainty. Red line shows the best-fit profile. Modeled mean age, $Be^{10}$ inheritance and erosion rate statistics are given at 2σ confidence level using analytical data listed in Table 4.**

[1]GSA Data Repository Item 2014057, DR1—Optically stimulated luminescence dating of sample OSL-PKV-2, is available at www.geosociety.org/pubs/ft2014.htm, or on request from editing@geosociety.org, Documents Secretary, GSA, P.O. Box 9140, Boulder, CO 80301-9140, USA.

TABLE 4. $^{10}$BE ANALYTICAL RESULTS FOR TCN-PKV-2 SAMPLE SITE IN PILOT KNOB VALLEY

| Sample name[a, b] | Depth to sample top (cm) | Thickness (cm) | Shielding factor[c] | Dissolved quartz (g) | Be carrier (g)[d] | $^{10}$Be/$^{9}$Be ($10^{-13}$)[e,f] | $^{10}$Be concentration ($10^{4}$ atoms g$^{-1}$ SiO$^{2}$)[g,h,i] |
|---|---|---|---|---|---|---|---|
| TCN-PKV-2.1 | 0 | 2 | 1 | 40.03 | 0.298 | 5.195 ± 0.149 | 24.94 ± 0.73 |
| TCN-PKV-2.2 | 14 | 3 | 1 | 40.10 | 0.316 | 4.653 ± 0.154 | 23.63 ± 0.80 |
| TCN-PKV-2.3 | 36 | 3 | 1 | 40.30 | 0.295 | 4.245 ± 0.153 | 19.96 ± 0.73 |
| TCN-PKV-2.4 | 65 | 4 | 1 | 40.04 | 0.301 | 2.784 ± 0.130 | 13.29 ± 0.64 |
| TCN-PKV-2.5 | 100 | 4 | 1 | 80.70 | 0.300 | 5.124 ± 0.182 | 12.28 ± 0.44 |
| TCN-PKV-2.6 | 175 | 4 | 1 | 61.63 | 0.313 | 2.096 ± 0.095 | 6.70 ± 0.32 |
| Blank 1 | – | – | – | – | 0.327 | 0.0973 ± 0.020 | – |
| Blank 2 | – | – | – | – | 0.306 | 0.0870 ± 0.013 | – |

[a] Samples consisted of 0.25-2.0 mm grains.
[b] Lab calibration blanks used to correct for background $^{10}$Be concentrations.
[c] No topographic shielding correction necessary at sample site (horizon <20° in all directions).
[d] Be carrier solution consists of a 995 ppm concentration and 1.013 g ml$^{-1}$ density.
[e] $^{10}$Be half-life of 1.387 Ma is used.
[f] Uncertainties reported at the 1σ confidence level.
[g] $^{10}$Be blank subtracted from sample.
[h] Five sediment samples constrain depth and density relationships: (1) 0 cm, 1.4 g cm$^{-3}$; (2) 18 cm, 1.7 cm$^{-3}$; (3) 26 cm, 2.3 g cm$^{-3}$; (4) 57 cm, 2.3 g cm$^{-3}$; and (5) 85 cm, 2.5 g cm$^{-3}$. Density is allowed to increase linearly with depth, but not exceed 2.5 g cm$^{-3}$.
[i] Total uncertainty is 1σ accelerated mass spectrometer error plus 2%.

along this segment of the fault ~40 km west of our site suggests that the most recent three events likely had offsets of 7 m, 7 m, and 4 m, respectively (McGill and Sieh, 1991). If these correspond to events seen in the paleoseismic record (Dawson et al., 2003), they would be consistent with slip rates on the order of 10.6–12.2 mm/yr during the past ~2 k.y. (Fig. 6). Collectively, these data support the contention that a relatively high slip rate is required to explain current velocity fields in terms of earthquake cycle stages (Chuang and Johnson, 2011). The discrepancy between our new Late Holocene slip-rate estimate and apparently low geodetic strain accumulation rates (~0–3 mm/yr, Bennett et al., 2003) may indicate that (1) the Garlock fault is late in its earthquake cycle (e.g., Chuang and Johnson, 2011; Peltzer et al., 2001) and/or (2) active strain accumulation has only recently focused along the Eastern California shear zone (Oskin et al., 2008).

The possibility that the Garlock fault is late in its earthquake cycle has important implications for seismic hazard characterization along the fault. McGill and Rockwell (1998) and Dawson et al. (2003) bracketed the last rupture of the central Garlock fault at Iron Canyon (Fig. 1) between A.D. 1450 and 1640. Assuming the Garlock fault has remained locked with no aseismic creep since this last event (ca. A.D. 1545), our late Holocene slip rate (9.3–12.5 mm/yr) would imply a slip deficit of 4.4–5.9 m. This is approximately double the implied deficit if the longer term slip rate of McGill and Sieh (1993) (5–7 mm/yr) is used. McGill and Sieh (1991) estimated that the Garlock fault has the potential to host a Mw 7.2–7.5 earthquake, if rupture involved 3–7 m of coseismic displacement along the central segment of the fault.

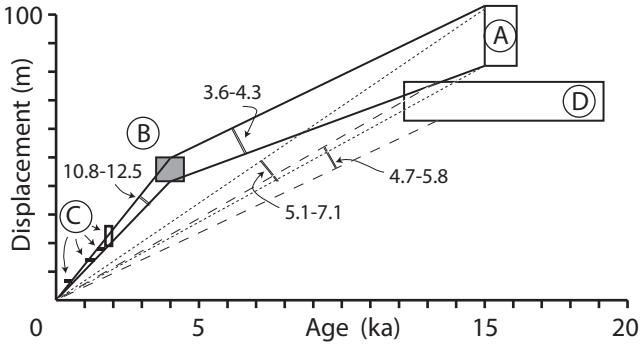


**Figure 6. Compilation of slip rate estimates from displaced geomorphic features along the central Garlock fault. Data sources are (A) displaced late Pleistocene shoreline and incised channel in southern Searles Valley (McGill and Sieh, 1993), (B) Late Holocene displacement presented in this study (shaded box), and (D) displaced late Pleistocene alluvial fan (Ganev et al., 2012). Average slip rates using late Pleistocene features are shown as finely dashed lines and yield estimates between ~5–7 mm/yr. Interval rates calculated considering our results (solid lines) suggest rates between 3.6 and 4.3 mm/yr in the late Pleistocene/early Holocene, but faster (10.8–12.5 mm/yr) during the late Holocene. A Qa3$_b$ mean age of 4 ka and a ca. 15 ka Searles Valley shoreline age are used to extrapolate slip rate intervals. Also plotted (C) are four paleoseismic events at Iron Canyon site (Dawson et al., 2003), displaying 7 m displacement for the most recent two events, 4 m for the third event, and a herein estimated 1–7 m hypothetical displacement for the oldest event. Predicted slip rates on the three most recent events (10.6–12.2 mm/yr) is consistent with late Holocene high slip rates (this study).**

## TECTONICS OF THE GARLOCK FAULT

Our results carry significant mechanical and kinematic implications for the interaction of the Garlock fault with both the Eastern California shear zone and the San Andreas system, and thus bears on complex transform plate boundaries in general. Accelerated slip along the fault since ca. 4 ka appears to correspond with a time period of lower seismic moment release along the Eastern California shear zone (e.g., Dolan et al., 2007). If temporal variations in slip rate along the Garlock fault are indeed coordinated with alternating periods of slip along different components of the North American plate boundary (Dolan et al., 2007), then they raise important questions about whether this interaction simply reflects the nature of fault interaction and elastic strain changes during earthquake clusters (e.g., Weldon et al., 2004), or whether nonsteady slip reflects strain hardening or weakening in the lower crust (e.g., Dolan et al., 2007; Oskin et al., 2008). Our documentation that the Garlock fault has experienced temporal variations in slip rate that average multiple earthquake cycles further supports a growing body of geodetic and paleoseismic evidence that attest to far-field coordinated interactions among the

fault systems marking the diffuse North American plate boundary.

Our results also support contentions that the present-day velocity field is influenced by earthquake cycle effects. In particular, our results are consistent with inference that the Garlock fault exhibits a relatively high slip rate (~9–11 mm/yr; Chuang and Johnson, 2011), but is relatively late in the earthquake cycle, such that differential velocities resolved along the fault are low (McClusky et al., 2001; Miller et al., 2001). Assuming that the high rate we determine for the Late Holocene presently characterizes the fault, and taking the timing of the most recent event documented in the paleoseismic record (Dawson et al., 2003), it is possible that the fault may have accumulated a slip deficit of 4–6 m. An event of this magnitude along the central and western segments of the Garlock fault would likely load faults in the Eastern California shear zone in Panamint and Death Valley (McAuliffe et al., 2013) and could enhance their potential for rupture.

## CONCLUSIONS

Our results provide the first documentation of time-variable slip rates on a major plate boundary fault in California. In Pilot Knob Valley, 30–50 m of displacement of a shutter ridge against a Late Holocene fan surface has been critically evaluated through mapping, analysis of both airborne and terrestrial LiDAR imagery, and trenching at key positions along the shutter ridge. The degree of soil development (3.1–3.6 PDI value; Table 1) and direct dating by OSL (4.07 ± 0.37 ka; Table 3 and Fig. 4) indicates that $Qa3_b$ deposition took place between 3.5 and 4.5 ka. Collectively, our results allow for Late Holocene slip rates between 6.7 and 14.3 mm/yr. However, our preferred reconstruction implies 43–50 m of displacement, and thus a most likely slip rate of 10.8–12.5 mm/yr during this time. Interval slip rates determined using displaced late Pleistocene Searles Lake shorelines reveal strongly time-variant slip histories that range from ~3.6–4.3 mm/yr during the Late Pleistocene and Early Holocene (15–4 ka), followed by a post-4 ka period of higher strain release. These large fluctuations of slip during the Holocene are likely linked to time-variant loading from faults in the Eastern California shear zone (e.g., Rockwell et al., 2000; Dolan et al., 2007).

### ACKNOWLEDGMENTS

This research was funded by the National Science Foundation Earthscope program (EAR 0643096) to Walker and Kirby. The authors would like to thank the Geothermal Program Office at the China Lake Naval Weapons station for field access. In particular, Dr. Frank Monastero, Dr. Andy Sabin, Dan McClung, and Steve Alm are owed tremendous gratitude for their help and hospitality. Tandis Bidgoli is thanked for her field assistance. We thank Mike Oskin and Sally McGill for insightful and constructive reviews that significantly improved the manuscript.

### REFERENCES CITED

Bacon, S.N., McDonald, E.V., Caldwell, T.G., and Dalldorf, G.K., 2010, Timing and distribution of alluvial fan sedimentation in response to strengthening of late Holocene ENSO variability in the Sonoran Desert, southwestern Arizona, USA: Quaternary Research, v. 73, p. 425–438, doi:10.1016/j.yqres.2010.01.004.

Bennett, R.A., Wernicke, B.P., Niemi, N.A., Friederich, A.M., and Davis, J.L., 2003, Contemporary strain rates in the northern Basin and Range province from GPS data: Tectonics, v. 22, 1008, 31 p, doi: 10.1029/2001TC001355.

Birkeland, P.W., 1999, Soils and geomorphology: Oxford University Press, New York, 430 p.

Bull, W.B., 1991, Geomorphic Responses to Climatic Change: Oxford University Press, Oxford, 326 p.

Chuang, R., and Johnson, K.M., 2011, Reconciling geologic and geodetic fault-slip-rate discrepancies in southern California: consideration of non-steady mantle flow and lower crustal fault creep: Geology, v. 39, p. 627–630, doi:10.1130/G32120.1.

Cowgill, E., 2007, Impact of riser reconstructions on estimation of secular variation in rates of strike-slip faulting: Revisiting the Cherchen River site along the Altyn Tagh fault, NW China: Earth and Planetary Science Letters, v. 254, p. 239–255, doi:10.1016/j.epsl.2006.09.015.

Davis, G.A., and Burchfiel, B.C., 1973, Garlock fault: An intracontinental transform structure, southern California: Geological Society of America Bulletin, v. 84, p. 1407–1422, doi:10.1130/0016-7606(1973)84<1407:GFAITS>2.0.CO;2.

Dawson, T.E., McGill, S.F., and Rockwell, T.K., 2003, Irregular recurrence of paleoearthquakes along the central Garlock fault near El Paso Peaks, California: Journal of Geophysical Research, v. 108, 2356, doi:10.1029/2001JB001744.

Dolan, J.F., Bowman, D.D., and Sammis, C.G., 2007, Long-range and long-term fault interactions in southern California: Geology, v. 35, p. 855–858, doi:10.1130/G23789A.1.

Galbraith, R.F., 1990, The radial plot: Graphical assessment of spread in ages. International Journal of Radiation Applications and Instrumentation. Part D: Nuclear Tracks and Radiation Measurements, v. 17, no. 3, p. 207–214, doi:10.1016/1359-0189(90)90036-W.

Galbraith, R.F., Roberts, R.G., Laslett, G.M., Yoshida, H., and Olley, J.M., 1999, Optical dating of single and multiple grains of quartz from Jinmium rock shelter, northern Australia: part I, experimental design and statistical models: Archaeometry, v. 41, no. 2, p. 339–364, doi:10.1111/j.1475-4754.1999.tb00987.x.

Gan, W., Zhang, P., Shen, Z.K., Prescott, W.H., and Svarc, J.L., 2003, Initiation of deformation of the Eastern California shear zone: constraints from Garlock fault geometry and GPS observations: Geophysical Research Letters, v. 30, 4 pp., doi: 10.1029/2003GL017090.

Ganev, P.N., Dolan, J.F., Frankel, K.L., and Finkel, R.C., 2010, Rates of extension along the Fish Lake Valley fault and transtensional deformation in the Eastern California shear zone - Walker Lane belt: Lithosphere, v. 2, p. 33–49, doi:10.1130/L51.1.

Ganev, P.N., Dolan, J.F., McGill, S.F., and Frankel, K.L., 2012, Constancy of geologic slip rate along the central Garlock fault: implications for strain accumulation and release in southern California: Geophysical Journal International, v. 190, p. 745–760, doi:10.1111/j.1365-246X.2012.05494.x.

Gile, L.H., Hawley, J.W., and Grossman, R.B., 1981, Soils and geomorphology in the Basin and Range area of southern New Mexico—guidebook to the Desert Project: New Mexico Bureau of Mines and Mineral Resources Memoir 39, 222 p.

Harden, J.W., 1982, A quantitative index of soil development from field descriptions: Examples from a chronosequence in central California: Geoderma, v. 28, p. 1-28.

Harden, J.W., and Taylor, E.M., 1983, A quantitative comparison of soil development in four climatic regimes: Quaternary Research, v. 20, p. 342–359, doi:10.1016/0033-5894(83)90017-0.

Helms, J.G., McGill, S.F., and Rockwell, T.K., 2003, Calibrated, late Quaternary age indices using clast rubification and soil development on alluvial surfaces in Pilot Knob Valley, Mojave Desert, southeastern California: Quaternary Research, v. 60, p. 377–393, doi:10.1016/j.yqres.2003.08.002.

Hidy, A.J., Gosse, J.C., Pederson, J.L., Mattern, J.P., and Finkel, R.C., 2010, A geologically constrained Monte Carlo approach to modeling exposure ages from profiles of cosmogenic nuclides: An example from Lees Ferry, Arizona: Geochemistry Geophysics Geosystems, v. 11, 18 p., doi: 10.1029/2010GC003084.

Lin, J.C., Broecker, W.S., and Hemming, S.R., 1998, A reassessment of U-Th and 14C ages for late-glacial high-frequency hydrological events at Searles Lake, California : Quaternary Research, v. 49, p. 11-23.

Machette, M.N., 1985, Calcic soils of the southwestern United States: Geological Society of America Special Paper 203, p. 1–22, doi: 10.1130/SPE203-p1.

Mahan, S.A., Miller, D.M., Menges, C.M., and Yount, J.C., 2007, Late Quaternary stratigraphy and luminescence geochronology of the northeastern Mojave desert: Quaternary International, v. 166, p. 61–78, doi:10.1016/j.quaint.2006.12.010.

McAuliffe, L.J., Dolan, J.F., Kirby, E., Rollins, C., Haravitch, B., Alm, S., and Rittenour, T.M., Paleoseismology of the southern Panamint Valley fault: Implications for regional earthquake occurrence and seismic hazard in southern California: Journal of Geophysical Research Solid Earth, v. 118, p. 1-21, doi: 10.1002/jgrb.50359.

McClusky, S.C., Bjornstad, S.C., Hager, B.H., King, R.W., Meade, B.J., Miller, M.M., Monastero, F.C., and Souter, B.J., 2001, Present day kinematics of the Eastern California Shear Zone from a geodetically constrained block model: Geophysical Research Letters, v. 28, p. 3369–3372, doi:10.1029/2001GL013091.

McDonald, E.V., McFadden, L.D., and Wells, S.G., 2003, Regional response of alluvial fans to the Pleistocene-Holocene climatic transition, Mojave Desert, California, *in* Enzel, Y., Wells, S.G., and Lancaster, N., eds., Paleoenvironments and Paleohydrology of the Mojave and Southern Great Basin Deserts: Geological Society of America Special Paper 368, p. 189–205, doi:10.1130/0-8137-2368-X.189.

McGill, S., and Rockwell, T., 1998, Ages of late Holocene earthquakes on the central Garlock fault near El Paso Peaks, California: Journal of Geophysical Research, v. 103, p. 7265–7 279, doi:10.1029/97JB02129.

McGill, S., and Sieh, K., 1991, Surficial offsets on the central and eastern Garlock fault associated with prehistoric earthquakes: Journal of Geophysical Research, v. 96, p. 21,597–21,621, doi:10.1029/91JB02030.

McGill, S., and Sieh, K., 1993, Holocene slip rate of the central Garlock fault in southeastern Searles Valley, California: Journal of Geophysical Research, v. 98, p. 14,217–14,231, doi:10.1029/93JB00442.

McGill, S.F., Wells, S.G., Fortner, S.K., Kuzma, H.A., and McGill, J.D., 2009, Slip rate of the western Garlock fault, at Clark Wash, near Lone Tree Canyon, Mojave Desert, California: Geological Society of America Bulletin, v. 121, p. 536–554, doi:10.1130/B26123.1.

Meade, B.J., and Hager, B.H., 2005, Block models of crustal motion in southern California constrained by GPS measurements: Journal of Geophysical Research, v. 110, 19 pp, doi: 10.1029/2004JB003209.

Miller, M.M., Johnson, D.J., Dixon, T.H., and Dokka, R.K., 2001, Refined kinematics of the Eastern California shear zone from GPS observations, 1993–1998: Journal of Geophysical Research, v. 106, 18 p.

Nicol, A., Walsh, J., Berryman, K., and Villamor, P., 2006, Interdependence of fault displacement rates and paleoearthquakes in an active rift: Geology, v. 34, p. 865–868, doi: 10.1130/G22335.1.

Numelin, T., Kirby, E., Walker, J.D., and Didericksen, B., 2007, Late Pleistocene slip on a low-angle normal fault, Searles Valley, California: Geosphere, v. 3, p. 163–176, doi:10.1130/GES00052.1.

Oskin, M., and Iriondo, A., 2004, Large-magnitude transient strain accumulation on the Blackwater fault, Eastern California shear zone: Geology, v. 32, p. 313–316, doi:10.1130/G20223.1.

Oskin, M., Perg, L., Shelef, E., Strane, M., Gurney, E., Singer, B., and Zhang, X., 2008, Elevated shear zone loading

rate during an earthquake cluster in eastern California: Geology, v. 36, p. 507–510, doi:10.1130/G24814A.1.

Peltzer, G., Crampe, F., Hensley, S., and Rosen, P., 2001, Transient strain accumulation and fault interaction in the Eastern California shear zone: Geology, v. 29, p. 975–978, doi:10.1130/0091-7613(2001)029<0975:TSAAFI>2.0.CO;2.

Pollitz, F.F., Wicks, C., and Thatcher, W., 2001, Mantle flow beneath a continental strike-slip fault: postseismic deformation after the 1999 Hector Mine earthquake: Science, v. 293, p. 1814–1818, doi:10.1126/science.1061361.

Rockwell, T.K., Lindvall, S., Herzberg, D., Murbach, D., Dawson, T., and Berger, G., 2000, Paleoseismology of the Johnson Valley, Kickapoo, and Homestead Valley faults: Clustering of earthquakes in the Eastern California shear zone: Bulletin of the Seismological Society of America, v. 90, p. 1,200–1,236.

Savage, J.C., Lisowski, M., and Prescott, W.H., 1990, An apparent shear zone trending north-northwest across the Mojave Desert into Owens Valley, Eastern California: Geophysical Research Letters, v. 17, p. 2113–2116.

Savage, J.C., and Prescott, W.H., 1978, Asthenosphere readjustment and the earthquake cycle: Journal of Geophysical Research, v. 83, p. 3369–3376, doi:10.1029/JB083iB07p03369.

Savage, J.C., Gan, W., and Svarc, J.L., 2001, Strain accumulation and rotation in the eastern California shear zone: Journal of Geophysical Research, v. 106, p. 21,995–22,007, doi:10.1029/2000JB000127.

Savage, J.C., Svarc, J.L., and Prescott, W.H., 2003, Near-field postseismic deformation associated with the 1992 Landers and 1999 Hector Mine, California earthquakes: Journal of Geophysical Research. Solid Earth, v. 108, doi:10.1029/2002JB002330.

Savage, J.C., Svarc, J.L., and Prescott, W.H., 2004, Interseismic strain and rotation rates in the northeast Mojave domain, eastern California: Journal of Geophysical Research, v. 109, p. B02406, doi:10.1029/2003JB002705.

Stein, R.S., 1999, The role of stress transfer in earthquake recurrence: Nature, v. 402, p. 605–609, doi:10.1038/45144.

Taylor, E., 1988, Instructions for the soil development index template: Lotus 1-2-3, USGS-OFR-88-233.

U.S. Geological Survey and California Geological Survey, 2006, Quaternary fault and fold database for the United States, http//earthquake.usgs.gov/regional/qfaults/ (accessed 11 May 2009).

Weldon, R., Scharer, K., Fumal, T., and Biasi, G., 2004, Wrightwood and the earthquake cycle: What a long recurrence record tells us about how faults work: GSA Today, v. 14, 4 pp., doi: 10.1130/1052-5173(2004)014<4:WATECW>2.0.CO;2.

MANUSCRIPT RECEIVED 18 MARCH 2013
REVISED MANUSCRIPT RECEIVED 7 NOVEMBER 2013
MANUSCRIPT ACCEPTED 18 NOVEMBER 2013

Printed in the USA